Tellus (2007), 59A, 599–617
Printed in Singapore. All rights reserved

TELLUS

Interdecadal changes in southern hemisphere winter storm track modes

By JORGEN S. FREDERIKSEN[1]* and CARSTEN S. FREDERIKSEN[2], [1]*CSIRO Marine and Atmospheric Research, PMB#1, Aspendale 3195, Victoria, Australia;*
[2]*Bureau of Meteorology Research Centre, GPO Box 1289, Melbourne 3001, Victoria, Australia*

(Manuscript received 27 April 2006; in final form 4 June 2007)

ABSTRACT

The interdecadal changes in southern hemisphere (SH) winter cyclogenesis have been studied using a global two-level primitive equation instability-model with reanalysed observed July three-dimensional basic states for the periods 1949–1968 and 1975–1994. The early to mid-1970s were a time of quite dramatic reduction in the winter rainfall in the southwest of western Australia (SWWA). We find that the rainfall reduction is associated with a decrease in the vertical mean meridional temperature gradient and in the peak upper tropospheric jet-stream zonal winds near 30° south throughout most of the SH. These changes are reflected in the properties of the leading SH cyclogenesis modes: for 1975–1994 both the fastest growing mode, and on average the 10 leading SH cyclogenesis modes that cross Australia, have growth rates which are around 30% smaller than for the corresponding modes for 1949–1968. The sensitivity of our results, to the strengths of physical parametrizations and to the choice of basic states based on different data sets, is examined.

Our results suggest that a primary cause of the rainfall reduction over SWWA in the period after 1975 is the reduction of the intensity of cyclogenesis and the southward deflection of some storms.

1. Introduction

The early to mid-1970s was a time of major shift in the structure of the large-scale circulation of both the northern and southern hemispheres (SH, Nitta and Yamada, 1989; Trenberth, 1990; Allan and Haylock, 1993). In the SH there was a dramatic reduction in winter rainfall in the southwest of western Australia (SWWA) associated with an increase in Perth mean sea level pressure (MSLP) (Sadler et al., 1988; Allan and Haylock, 1993; IOCI, 2002). In fact, approximately 60% of the variance in SWWA winter rainfall is explained by fluctuations in Perth MSLP throughout the 1900s (Smith et al., 2000, and references therein). As well there are significant correlations between mainly inland WA winter rainfall and Indian Ocean sea surface temperatures (SSTs) (Nicholls, 1989; Drosdowsky, 1993; Smith, 1994; Smith et al., 2000).

In the Northern Hemisphere the Pacific-North American teleconnection pattern became more dominant and persistent in winter after the 1970s with lower geopotential height at 500 hPa over the North Atlantic (Nitta and Yamada, 1989; Trenberth, 1990). These atmospheric circulation changes in the Northern Hemisphere have been related to an El Niño type response in the Pacific Ocean with warmer SSTs in the eastern tropical Pacific compared with the western part of the ocean (Nitta and Yamada, 1989; Trenberth, 1990; Meehl and Washington, 1996) and this response operates on an interdecadal time scale (Zhang et al., 1997). This so called Pacific Decadal Oscillation (PDO) or Interdecadal Pacific Oscillation (IPO) also modulates Australian climate, particularly on the east coast (Power et al., 1999; Arblaster et al., 2002). It has been suggested that both internal natural variability of the coupled ocean atmosphere system and enhanced greenhouse gas induced climate change may be responsible for recent interdecadal changes in tropical Pacific Ocean SSTs and associated circulation and rainfall changes (Meehl and Washington, 1996; Knutson and Manabe, 1998). Indeed, from the work of Leith (1975) employing the fluctuation–dissipation theorem and from more recent numerical studies (e.g. Brandefelt and Källén, 2004 and references therein) one would expect anthropogenic forcing to project onto the leading modes of natural climate variability.

In contrast to the situation for the eastern Australia, there is considerably less correlation between the Southern Oscillation Index (SOI) or the PDO and circulation and rainfall over SWWA (Smith et al., 2000 and references therein). Thus, attributing the

*Corresponding author.
e-mail: Jorgen.Frederiksen@csiro.au
DOI: 10.1111/j.1600-0870.2007.00264.x

causes, either natural or anthropogenic, of the winter circulation and rainfall changes since the 1970s in SWWA is problematic and there appears as yet no generally accepted explanation. Our purpose here is not to address this important but difficult question but to examine a second key issue, namely, the relationships between the observed changes in the mean basic state climate, before and after the mid-1970s, and the consequent changes in the transient dynamic disturbances that may be responsible for the reduction in SWWA rainfall. In this paper, we examine this relationship by analysing the dynamic transients that result from the instability of observed July basic states taken from periods before and after the 1970s shift in the atmospheric circulation. Our aim is to explore whether the primary causes of the changed rainfall is due to changes in the growth rate, strength or location of extratropical storms. There have previously been a number of observational and modelling studies performed on the variability of SH extratropical cyclone activity in nature and in general circulation model simulations with anthropogenic greenhouse forcing (e.g. Simmons and Keay 2000a, b; Fyfe 2003; Brandefelt and Källén 2004). We relate our results to these works, although their focus has been on changes in storm track activity south of 40°S rather than over southern Australia, as well as to the climatological study of southern Australian low pressure systems by Qi et al. (1999).

Previous observational studies have detailed the close relationship between the growth (or deepening) rate of extratropical cyclones and their periods of development and rainfall intensity. Sanders and Gyakum (1980) and Roebber (1984) found that rapidly deepening storms have longer periods of development than slower growing storms, with preferential development favoured just downstream of the planetary wave trough and maximum baroclinicity (Frederiksen, 1992). Petty and Miller (1995), McMurdie and Katsaros (1996) and Martin and Otkin (2004) find strong correlations between deepening rates of storms and precipitation with heavy bursts of precipitation occurring during the development stage of rapidly growing storms. Here we use instability theory to examine the growth rates of storms growing on the SH winter flow before and after the mid-1970s.

During the last two decades it has been shown that instability theory with observed basic states that have both horizontal and vertical variations in the flow fields can explain the generation mechanisms and dynamic properties of the major classes of synoptic- and large-scale atmospheric disturbances. The causes of localized cyclogenesis and the structures of the major storm tracks in both the Northern (Frederiksen, 1982, 1983a; Frederiksen and Frederiksen, 1992; Whitaker and Barcilon, 1992; Lee, 1995; Whitaker and Dole, 1995; Hall and Sardeshmukh, 1998) and Southern (Frederiksen, 1985; Frederiksen and Frederiksen, 1993a) Hemispheres have been explained. In particular, it was shown that the theoretical predictions of the geographical structures of SH storm tracks, and their seasonal variations, agree closely with observations (Trenberth, 1981, 1991). It has also been possible to explain the dynamic causes of many other atmospheric phenomena including blocking and teleconnection patterns (Frederiksen, 1982, 1983b; Simmons et al., 1983; Branstator, 1985; Anderson, 1991; Frederiksen and Frederiksen, 1993a; Branstator and Held, 1995; Frederiksen and Branstator, 2001), intraseasonal oscillations and convectively coupled equatorial waves (Frederiksen and Frederiksen, 1993b, 1997; Frederiksen, 2002) and Australian northwest cloud band disturbances (Frederiksen and Frederiksen, 1996). For our current studies of the transient instabilities growing on July global basic states for 1949–1968 and 1975–1994 we employ the two-level linearized primitive equation model that was developed and applied in the series of studies by Frederiksen and Frederiksen (1992, 1993a, b, 1997) (hereafter FF92, FF93a,b, FF97, respectively) and by Frederiksen (2002). The current version of the model includes a generalized Kuo-type heating parametrization that incorporates closures for both convection and evaporation-wind feedback, as outlined in Frederiksen (2002). We include the evaporation-wind feedback parametrization since we perform a global calculation including the tropics where it may significantly affect some of the instability modes, although our primary focus here is on storm tracks. The model has been shown to yield SH storm track modes that have very similar structures and growth rates to those for the five-level quasigeostrophic model of Frederiksen (1985 and references therein) for suitable dissipation parametrizations. It has however the advantage that the static stability varies with geographical location and it incorporates parametrizations of convective heating and evaporation-wind feedback.

The plan of this paper is as follows. Section 2 contains a summary of the two-level primitive equation instability model used in this work and details the specification of the generalized Kuo-type parametrization including closures for convective heating and evaporation-wind feedback. Section 3 describes the averaged basic states for July 1949–1968 and 1975–1994 used in our study while in Section 4 we compare instability criteria for cyclogenesis for the two basic states. In Section 5, we examine the growth rates and periods of the 20 fastest growing modes for the two basic states and focus on comparisons of the growth rates and periods of the leading SH cyclogenesis modes. In Section 6, we compare and contrast the structures and amplitudes of leading SH cyclogenesis modes for the two periods and relate their properties to the causes of the rainfall reduction over SWWA in the period 1975–1994. In Section 7, we examine the sensitivity of our results to the strength of the convection, surface evaporation and dissipation and to the choice of basic states based on different data sets. Our conclusions are presented in Section 8. The Appendix summarizes the formulation of the generalized Kuo-type parametrization used in this study.

2. Model details

The transient instabilities analysed in this study have been obtained using the two-level linearized primitive equation model

that was developed and applied in a series of studies by Frederiksen and Frederiksen (1992, 1993a, b, 1997) and by Frederiksen (2002). The current version of the model includes a generalized Kuo-type heating parametrization that incorporates closures for both convection and evaporation-wind feedback, as outlined in Frederiksen (2002) and formulated in more detail in our Appendix. The linearized primitive equations are described in terms of a mean perturbation streamfunction ψ, which is the average between the values at the upper (level 1) and lower (level 3) levels, a vertical shear perturbation streamfunction τ, which is half the difference between the upper- and lower-level values, the lower-level perturbation velocity potential χ (equal to minus the upper-level velocity potential), and the mean and vertical shear perturbation potential temperatures θ and σ, respectively.

We consider a heating profile for which the generalized Kuo-type heating projects completely onto the internal mode dynamics (see Appendix). The heating due to convection and surface evaporation then only enters the linearized mean potential temperature equation and is given by

$$\tilde{Q}_\theta = -\bar{s}\nabla^2\chi + C_F[u^{(3)} f_u + v^{(3)} f_v], \tag{1}$$

where the basic state moisture destabilization parameter is

$$\bar{s} = A_F m L \bar{q}/c_p = Q_F \bar{q}, \tag{2}$$

and the evaporation structure functions are:

$$f_u = \frac{(\bar{q}_s - \bar{q})\bar{u}^{(3)}}{\{[\bar{u}^{(3)}]^2 + [\bar{v}^{(3)}]^2\}^{1/2}}, \tag{3a}$$

$$f_u = \frac{(\bar{q}_s - \bar{q})\bar{v}^{(3)}}{\{[\bar{u}^{(3)}]^2 + [\bar{v}^{(3)}]^2\}^{1/2}}. \tag{3b}$$

Here the parameters C_F and A_F are given by eqs (A.16) and (A.17), respectively and Q_F is an effective convective heating parameter defined in eq. (A.15). Also, $u^{(3)}[u^{(-3)}]$ and $v^{(3)}[\bar{v}^{(-3)}]$ are the lower-level zonal and meridional perturbation (basic state) velocities; $\bar{q}$ and $\bar{q}_s$ are the basic state specific humidity and saturation specific humidity at the lower-level, respectively; L is the latent heat of condensation and m is the moisture availability factor (see Appendix). We assume that $\bar{q}$ is essentially equivalent to the moisture mixing ratio $\bar{W}$.

The first term in eq. (1) is the convection parametrization which, in this linearized form, gives heating for rising motion and cooling for sinking motion. The second term in eq. (1) is the evaporation-wind feedback mechanism. It is slightly more general than that used by Neelin et al. (1987) in that it involves both the zonal and meridional winds. With these closures included, the linearized mean perturbation potential temperature equation becomes

$$\begin{aligned}\frac{\partial\theta}{\partial t} &= -J(\bar{\psi},\theta) - J(\psi,\bar{\theta}) - J(\bar{\tau},\sigma) - J(\tau,\bar{\sigma}) \\ &\quad + \nabla\cdot\bar{\sigma}\nabla\chi + \nabla\cdot\sigma\nabla\bar{\chi} - K'\nabla^4\theta - \bar{s}\nabla^2\chi \\ &\quad + C_F[u^{(3)} f_u + v^{(3)} f_v],\end{aligned} \tag{4a}$$

where the overbar refers to the basic state. The equations for the other perturbation fields ψ, τ, χ and σ are given by:

$$\begin{aligned}\frac{\partial\nabla^2\psi}{\partial t} &= -J(\bar{\psi},\nabla^2\psi) - J\left(\psi,\nabla^2\bar{\psi} + 2\mu + \frac{1}{2}h\right) \\ &\quad - J(\bar{\tau},\nabla^2\tau) - J\left(\tau,\nabla^2\bar{\tau} - \frac{1}{2}h\right) + J(\bar{\chi},\nabla^2\chi) \\ &\quad + J(\chi,\nabla^2\bar{\chi}) + \nabla\cdot\left[\left(\nabla^2\bar{\tau} - \frac{1}{2}h\right)\nabla\chi\right] \\ &\quad + \nabla\cdot(\nabla^2\tau\nabla\bar{\chi}) + \nabla\cdot(\nabla^2\bar{\chi}\nabla\tau) + \nabla\cdot(\nabla^2\chi\nabla\bar{\tau}) \\ &\quad - K\nabla^2(\psi - \tau) - K'\nabla^6\psi,\end{aligned} \tag{4b}$$

$$\begin{aligned}\frac{\partial\nabla^2\tau}{\partial t} &= -J\left(\bar{\psi},\nabla^2\tau\right) - J\left(\psi,\nabla^2\bar{\tau} - \frac{1}{2}h\right) \\ &\quad - J\left(\bar{\tau},\nabla^2\psi\right) - J\left(\tau,\nabla^2\bar{\psi} + 2\mu + \frac{1}{2}h\right) \\ &\quad + \nabla\cdot\left((\nabla^2\bar{\psi} + 2\mu + \frac{1}{2}h)\nabla\chi\right) + \nabla\cdot\left(\nabla^2\psi\nabla\bar{\chi}\right) \\ &\quad + K\nabla^2(\psi - \tau) - K'\nabla^6\tau,\end{aligned} \tag{4c}$$

$$\begin{aligned}\frac{\partial\nabla^2\chi}{\partial t} &= -J\left(\bar{\chi},\nabla^2\psi\right) - J\left(\chi,\nabla^2\bar{\psi} + 2\mu + \frac{1}{2}h\right) \\ &\quad - \nabla\cdot\left((\nabla^2\bar{\psi} + 2\mu + \frac{1}{2}h)\nabla\tau\right) - \nabla\cdot(\nabla^2\psi\nabla\tau) \\ &\quad - \nabla\cdot\left((\nabla^2\bar{\tau} - \frac{1}{2}h)\nabla\psi\right) - \nabla\cdot\left(\nabla^2\psi\ \nabla\ \bar{\tau}\right) \\ &\quad + \nabla^2(\nabla\bar{\psi}\cdot\nabla\tau + \nabla\psi\cdot\nabla\bar{\tau} - J(\bar{\psi},\chi) \\ &\quad - J(\psi,\bar{\chi}) + \theta) - K\nabla^2\chi - K'\nabla^6\chi,\end{aligned} \tag{4d}$$

$$\begin{aligned}\frac{\partial\sigma}{\partial t} &= -J\left(\bar{\psi},\sigma\right) - J\left(\psi,\bar{\sigma}\right) - J\left(\bar{\tau},\theta\right) - J\left(\tau,\bar{\theta}\right) \\ &\quad + \nabla\cdot\bar{\theta}\nabla\chi + \nabla\cdot\theta\nabla\bar{\chi} - K'\nabla^4\sigma.\end{aligned} \tag{4e}$$

Here the Jacobian

$$J(X,Y) = \frac{\partial X}{\partial\lambda}\frac{\partial Y}{\partial\mu} - \frac{\partial X}{\partial\mu}\frac{\partial Y}{\partial\lambda} \tag{5}$$

and λ is longitude, μ is sine of latitude ϕ and t is time. The strength of the diffusion is specified by K and K' which denote surface drag and bi-harmonic diffusion coefficients, respectively. Also $h = 2\mu g A H/(RT_0)$, where H is the global topography as shown in fig. 1d of FF93a, g is the gravitational acceleration, R is the gas constant for air, T_0 is the horizontally averaged surface temperature, and A is a vertical profile factor taken to be 1.

These equations have been non-dimensionalized by using a, the radius of the earth, as a length scale; Ω^{-1}, the inverse of the earth's angular speed of rotation, as a time scale; and $a^2\Omega^2/b_\kappa c_p$ as a temperature scale, where c_p is the specific heat at constant pressure and $b_\kappa = 0.124$ is a dimensionless constant. Corresponding dimensional quantities are indicated by the superscript d in the sequel.

Again, each of the perturbation fields and basic state fields is expanded in terms of spherical harmonics with the perturbations also having a time dependence $\exp(-i\omega t)$. Here t is the time and $\omega = \omega_r + i\omega_i$ is the complex angular frequency with ω_r being the frequency and ω_i the growth rate. This then results in a system of eigenvalue–eigenvector equations of the form

$$-i\omega x = \boldsymbol{A}x \tag{6a}$$

where

$$x = (\ldots, \psi_{mn}, \ldots, \tau_{mn}, \ldots, \chi_{mn}, \ldots, \theta_{mn}, \ldots, \sigma_{mn}, \ldots)^T \tag{6b}$$

is the column vector of spherical harmonic spectral coefficients of the five field variables, T denotes transpose, and the matrix $\boldsymbol{A}$ is determined as described in FF92. In general, the eigen modes together with their adjoint modes form a complete biorthogonal system for representing any disturbance (Frederiksen and Bell, 1990). A rhomboidal 15 truncation is used for both the perturbation and basic state fields in which the zonal wavenumber $m = -15, \ldots, 0, \ldots, 15$ and the total wave number $n = |m|, |m|+1, \ldots, |m|+15$. This resolution is adequate for resolving the leading storm track modes and lower frequency modes of variability. Studies of the relationship between resolution and the dissipation required to obtain the same large-scale flow properties, predictability and instability have been carried out by Frederiksen and Kepert (2006, and references therein). Here we examine the instability properties for a range of dissipations to draw general conclusions.

3. Basic states

For the results presented in the next three sections, the source of the observed fields is the National Centres for Environmental Prediction/National Center for Atmospheric Research (NCEP/NCAR) reanalysis project (Kalnay et al., 1996). We must recognize there are limitations in accuracy as well as spatial and temporal inhomogeneities in fields derived by combining model output with raw observations of non-uniform quality and coverage (Hines et al., 2000; Simmons et al., 2004). For this reason we also examine, in Section 7, the sensitivity of our results to using basic states based on the European Centre for Medium Range Weather Forecasting (ECMWF) Reanalysis (ERA-40) project (Kållberg et al., 2004). There we also examine how our results depend on the number of years in the averaging periods.

We focus, in the next three sections, on the global SH mean July climate fields for the periods 1949–1968 and 1975–1994, based on NCEP/NCAR data, and find that there are significant differences between the two periods. Most notable is a reduction of 17% in the peak strength of the SH subtropical jet stream (Fig. 1).

Figure 1 shows the height (in pressure units) and latitudinal cross-section of the zonal wind, averaged over 100°E–130°E longitude. In both periods, there is a maximum in the zonal wind strength in the subtropics (near 30°S) at about the 200 hPa pressure level. In the later period, there is a reduction in the zonal wind of up to 9.4 m s^{-1} in this maximum. As well we note the increase in the zonal wind, particularly in the upper troposphere, near 45°S and in the main northern hemisphere jet core near 35°N. These changes are directly associated with changes in the Hadley circulation (not shown) including a reduction in the strength of the downward branch near the SH jet core. There have also been substantial changes in the Walker circulation with

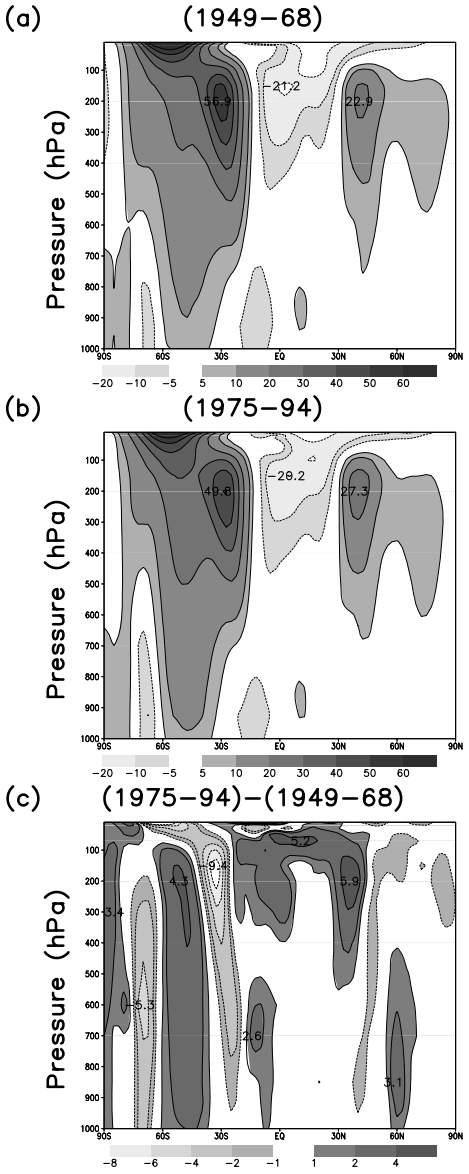

Fig. 1. Vertical cross-section of July zonal wind (m s^{-1}) averaged between 100° and 130°E as a function of latitude and pressure (in hPa) for the 1949–1968 basic state (a), the 1975–1994 basic state (b) and their difference (1975–1994)–(1949–1968) (c). Contour intervals are 10, 10 and 2 m s^{-1}, respectively, but here and in subsequent figures, may be closer spaced near 0 as shown on bars.

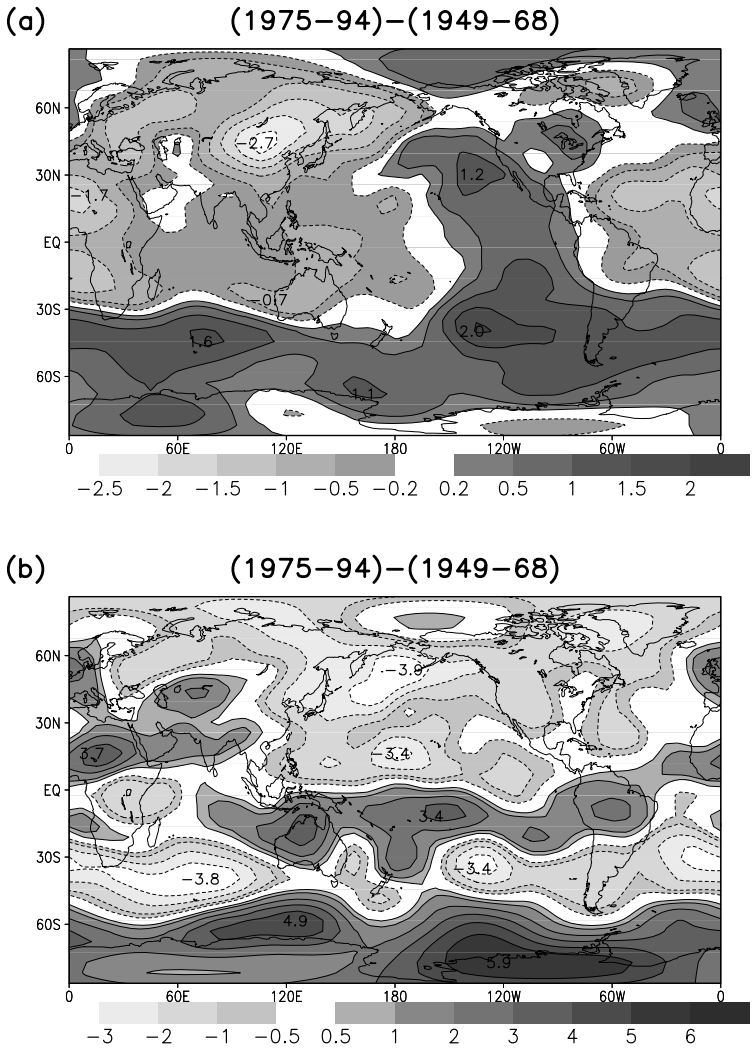

Fig. 2. Horizontal latitude–longitude plot of the July (1975–1994)–(1949–1968) difference in the vertically averaged potential temperature (K) (a) and the corresponding vertically averaged streamfunction difference ($km^2\ s^{-1}$)(b). Contour intervals are 0.5 K and 1 $km^2\ s^{-1}$, respectively.

increased upper level wind divergence in the eastern tropical Pacific in the latter period (not shown).

The thermal structure of the SH atmosphere has also changed with a significant warming south of 30°S, as shown in the vertically averaged temperature difference between the two periods in Fig. 2a. This has reduced the equator-to-pole temperature gradient particularly in the eastern hemisphere. As well the difference in the vertically average streamfunction between the two periods is associated with a change in the strength of the Antarctic Oscillation, also known as the high-latitude mode or southern hemisphere annular mode (Kidson, 1988; Marshall et al., 2004), as shown in Fig. 2b. It has also been found that there is a trend in the southern hemisphere annular mode in many simulations of transient greenhouse warming (Fyfe et al., 1999; Cai et al., 2003; Brandefelt and Källén, 2004).

The above-mentioned changes would be expected to have a significant effect on the stability of the SH circulation and hence on the nature of the SH storms and other modes of weather variability. In fact, as detailed in this study, in the period 1975–1994 the SH atmosphere has generally become less unstable in those regions associated with the generation of mid-latitude storms. On the basis of the discussion in Section 1, we would expect associated reductions in rainfall during the latter period. We have calculated the July rainfall change between (1975–1994) minus (1949–1968) (not shown). We find that the winter rainfall is reduced in central Australia and particularly in the high winter rainfall area of SWWA and across Victoria and along the east coastal belt of southeastern Australia to central Queensland.

The flow fields for the basic states that we focus on in the next three sections are the monthly averaged July global fields for the periods 1949–1968 and 1975–1994 from the NCEP/NCAR reanalyses. We use global 300- and 700-hPa fields as representative of the upper- and lower-levels, respectively and the fields of streamfunction, velocity potential and potential temperature are represented as rhomboidal wavenumber 15 spectral fields as described in FF93a. For each of the two basic states the SH

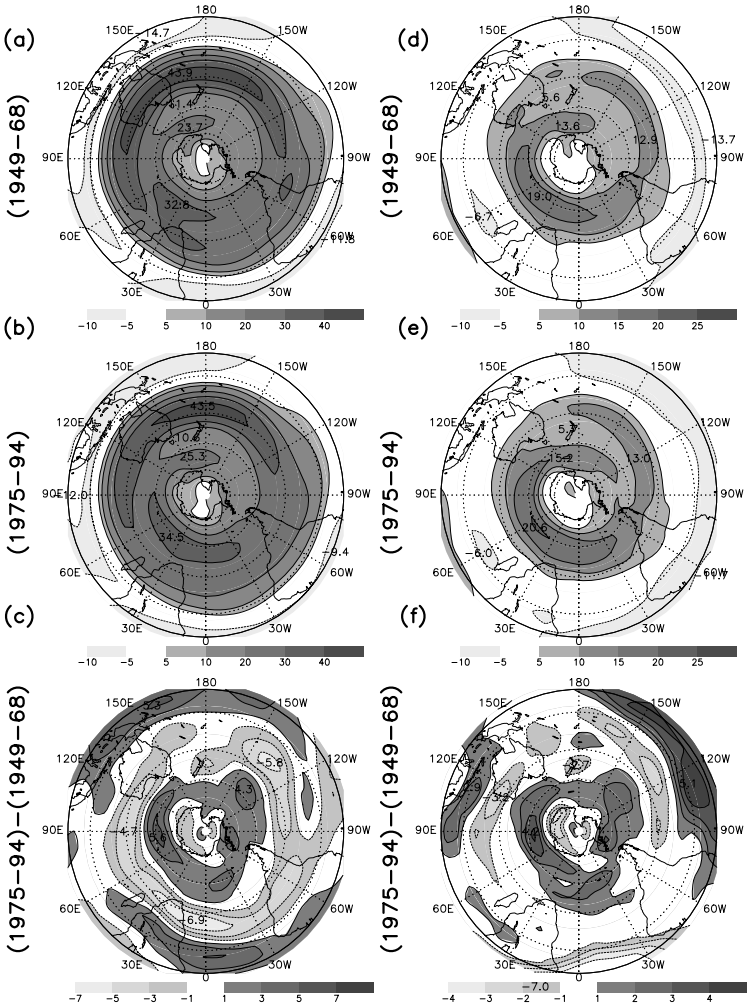

Fig. 3. The SH upper-level basic state zonal wind $u^{(1)d}$ (m s^{-1}), taken from 300-hPa observations, for July 1949–1968 (a), 1975–1994 (b) and the (1975–1994)–(1949–1968) difference (c). The lower-level basic state zonal wind $u^{(3)d}$ (m s^{-1}), taken from 700-hPa observations, for July 1949–1968 (d), 1975–1994 (e) and the (1975–1994)–(1949–1968) difference (f). Contour intervals are 10, 10, 2, 5, 5 and 1 m s^{-1}, respectively.

300- and 700-hPa zonal winds are shown in Fig. 3 as are the corresponding changes in these winds between the two periods. We note in particular (Fig. 3a) the strong jet stream at 300-hPa stretching across southern Australia between 80°E and 120°W longitude and centred on 30°S in the 1949–1968 data. For the 1975–1994 basic state the subtropical jet at 300-hPa is generally weaker (Fig. 3b). The 300-hPa difference in Fig. 3c shows that the reduction in the zonal wind in the later period, of up to 7 m s$^{-1,}$ extends across essentially the whole hemisphere in a band centred near 30°S. As well, there is a band to the south centred near 50°S with increases of up to 5.6 m s^{-1}. Again, these changes and corresponding changes at 700-hPa (Figs. 3d–f) are quite dramatic and representative of the systematic change that has occurred in the SH climate since the early to mid-1970s.

The transient perturbation modes experience the effects of the instability of the three-dimensional basic state fields and of convection, surface evaporation feedback, topography and dissipation. The global topography is shown in fig. 1d of FF93a and the scale height for the topography is as described in Section 2. We use drag and bi-harmonic diffusion coefficients with values

$$K^d = 8.39 \times 10^{-7}\ \mathrm{s}^{-1}, \tag{7}$$

$$K'^d = 2.338 \times 10^{16}\ \mathrm{m}^4\mathrm{s}^{-1} \tag{8}$$

as in our previous studies.

The strength of the convective heating (eqs 1 and A.15), is specified by

$$Q_F^d = 1500K \tag{9}$$

and the corresponding moisture destabilization parameter $\bar{s}$ is positive (eq. 2). For a slowly varying basic state static stability we can combine the moisture destabilization parameter with the dry static stability term in eq. (4a) and define a moist static stability by

$$\bar{\sigma}_m = \bar{\sigma} - \bar{s}. \tag{10}$$

Thus the convective parametrization, which is our representation cumulus heating in the tropics and convective processes in the extratropics, results in an effective reduction in the static stability.

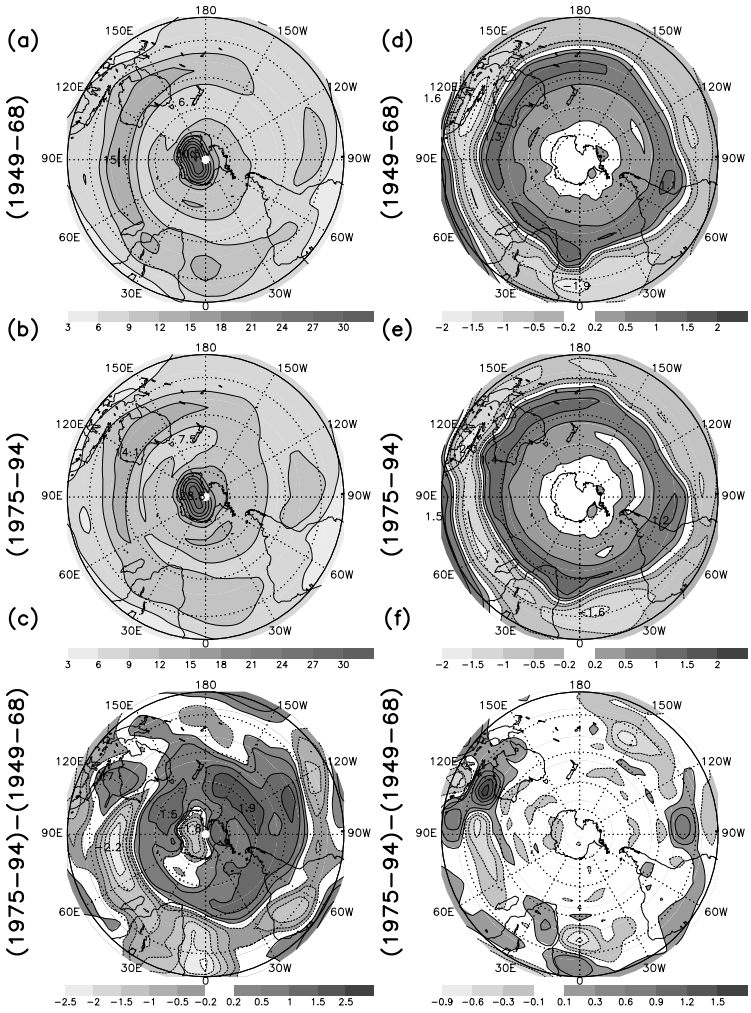

Fig. 4. The SH moist static stability parameter $\sigma_m^d = \sigma^d - s^d$ (K) of eq. (10) for July 1949–1968 (a), 1975–1994 (b) and the (1975–1994)–(1949–1968) difference (c). The SH evaporation-wind structure function f_u^d (g kg^{-1}) of eq. (3a) for July 1949–1968 (d), 1975–1994 (e) and the (1975–1994)–(1949–1968) difference (f). Results are for $Q_F^d = 1500$ K and $C_F^d = 5 \times 10^{-4}$ Km^{-1}. Contour intervals are 3, 3, 1, 0.5, 0.5 and 0.3, respectively.

The SH moist static stability is shown in Figs. 4a–c, respectively for the 1949–1968 and 1975–1994 basic states and their difference. We note that the differences in the moist static stability for the two periods is relatively minor and is therefore not expected to be as important a determinant of changes in transient instabilities as the zonal winds (Fig. 3) and horizontal temperature structure (Fig. 2a).

The strength of the evaporation-wind feedback (eq. 1) is specified by

$$C_F^d = 5 \times 10^{-4}\,\mathrm{Km}^{-1} \tag{11}$$

as in Frederiksen (2002). It should be noted that C_F^d in Km^{-1} has similar magnitudes to the non-dimensional drag coefficient for evaporation C_E (eq. A.6b) and is identical when the Kuo parameter $(1 - b) = 0.8$ (eq. A.16). The evaporation-wind structure function f_u^d has most effect on the transient instabilities in general while f_v^d has less systematic effect as discussed in more detail in Frederiksen (2002). The function f_u^d in grams per kilograms is shown in Figs. 4d–f, respectively for the 1949–1968 and 1975–1994 basic states and their difference. We note that, as expected, f_u^d has a similar structure to the corresponding 700-hPa zonal wind for each of the basic states shown in Fig. 3 but is more confined to the subtropics. In the SH there is in general little difference in f_u^d between the two periods apart from the increased evaporation off the northwest coast of Australia after 1975.

Throughout this paper strengths of the dissipation, convection and evaporation-wind feedback take the values specified above (eqs 7–9 and 11) (and these are denoted the 'standard parametrization'), except where stated otherwise; in particular, in Section 7, we consider the sensitivity of our results to these parametrizations.

4. Instability criterion for cyclogenesis

Before carrying out the full instability calculation with the model described in Section 2 it is perhaps of interest to examine the regions of likely cyclogenesis based on the simple criterion of Phillips (1954) generalized for a moist static stability $\bar{\sigma}_m^d$ and spherical geometry as used in FF93a. This criterion may be written as

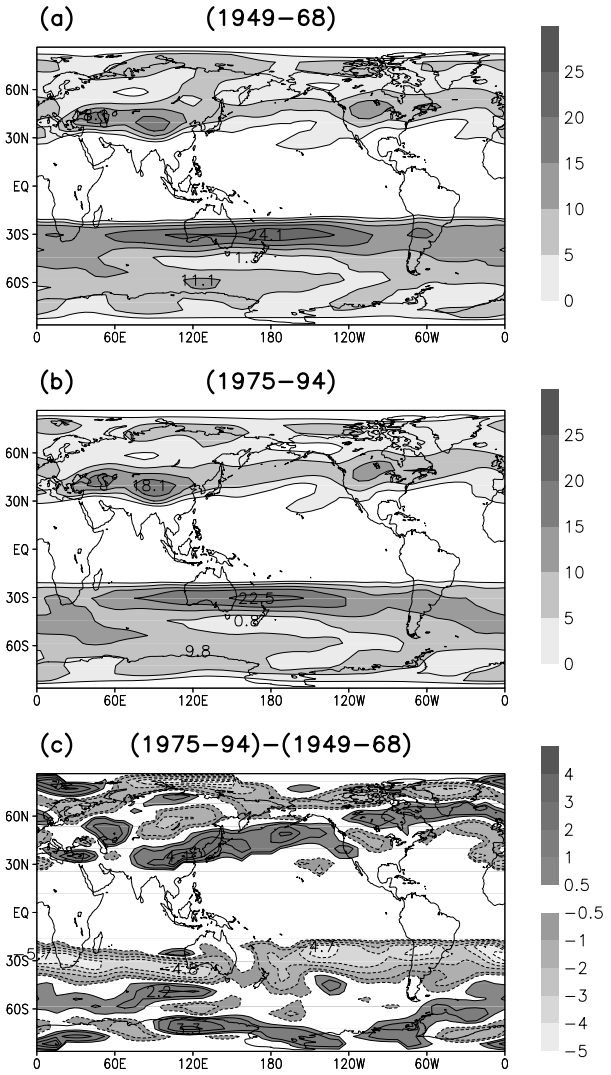

Fig. 5. The global generalized Phillips instability criterion of eq. (12), with the moist static stability $\bar{\sigma}_m^d$ and $Q_F^d = 1500$ K, in units of m s^{-1} for July 1949–1968 (a), 1975–1994 (b) and the (1975–1994)–(1949–1968) difference (c). Contour intervals are 5, 5 and 1, respectively.

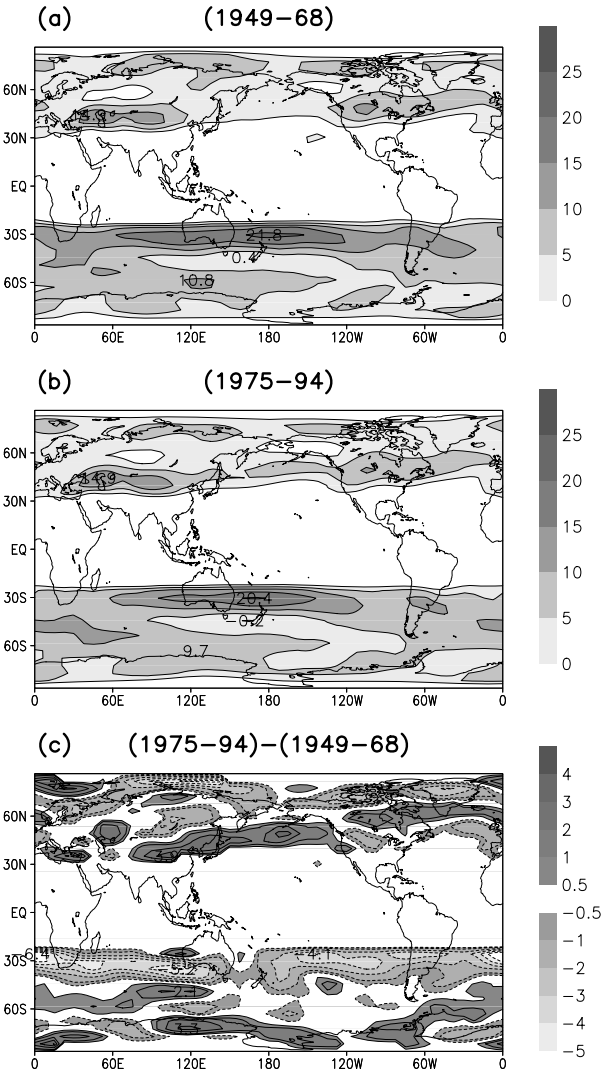

Fig. 6. As in Fig. 5 with the dry static stability $\bar{\sigma}^d$.

$$\bar{u}^{(1)d} - \bar{u}^{(3)d} - \frac{b_\kappa c_p \bar{\sigma}_m^d}{a\Omega} \frac{(1-\mu^2)^{1/2}}{\mu^2} \geq 0, \tag{12}$$

where $\bar{u}^{(1)d}$ and $\bar{u}^{(3)d}$ are the upper and lower level total zonal velocities. The fact that the denominator contains the factor $\mu^2 = \sin^2 \phi$ means that near the equator the criterion will always be negative and thus the criterion is primarily of relevance for the development of extra-tropical cyclogenesis. In Figs. 5a–c we show the regions where the instability criterion is positive for the 1949–1968 and 1975–1994 basic states and their difference, respectively. We note the close structural similarity between the instability criteria and the corresponding extra-tropical 300-hPa zonal winds shown in Fig. 3. Again we would expect a reduction of cyclogenesis in a band around 30°S extending longitudinally across most of the SH including SWWA. In fact, whether the moist static stability $\bar{\sigma}_m^d$ is used in the definition of the Phillips criterion or the corresponding dry static stability $\bar{\sigma}^d$ is employed does not change our general conclusions. This may be seen by comparing Fig. 5 with the corresponding dry criteria in Fig. 6. We note that while the instability is predicted to be stronger with the moist static stability in Figs. 5a and b compared with the dry static stability in Figs. 6a and b, as expected, the differences between 1975–1994 and 1949–1968 are very similar (Figs. 5c and 6c).

5. Growth rates, periods and pattern correlations

The large eigenvalue–eigenvector problem (6a) (with a 2480 × 2480 matrix) has been solved for both the 1949–1968 and 1975–1994 basic states including the parametrizations described

in Section 3. As in our previous studies a wide variety of modal disturbances that can be related to many aspects of atmospheric dynamics have been obtained. Here, however, our focus will be on SH cyclogenesis modes that are amongst the 20 fastest growing modes for each basic state since it is for these modes that the changes are the most dramatic.

Table 1 gives the mode number, period and e-folding times of the 20 leading modes for the 1949–1968 basic state while Table 2 gives the corresponding results for the 1975–1994 basic state. Also shown are the mode types and the largest pattern correlations between modes for the two basic states. Here the pattern correlations shown are the maximum over the phases of the modes and (the averages) taken over the five model fields ψ, τ, χ, θ and σ. The pattern correlations of the perturbation fields are calculated as described in appendix C of Frederiksen and Bell (1990). For a good fit, the pattern correlations as calculated require that both the real and imaginary parts of the two modes of interest are similar; this ensures that two travelling modes are similar throughout their evolution.

Table 1 shows that the leading mode for the 1949–1968 basic state is a SH cyclogenesis mode and that many of the modes among the first 20 fastest growing also correspond to SH cyclogenesis. The most similar disturbance to mode1 for the 1949–1968 basic state is mode 9 for the 1975–1994 basic state and they have a pattern correlation of just over 0.9. However, mode 9 for 1975–1994 has a growth rate that is 33% less than mode 1 for 1949–1968. We also note from Tables 1 and 2 that there are considerable fewer SH cyclogenesis modes amongst the first 20 fastest growing modes for 1975–1994 than for 1949–1968. In fact, on average the 10 leading SH cyclogenesis modes for 1975–1994, most of which cross Australia have growth rates that are 32% smaller than for the corresponding modes for 1949–1968. Those that slip to the south of the Australian continent are largely unaffected.

We also note from Table 1 that for 1949–1968 the first 20 modes correspond to southern and northern hemisphere cyclogenesis modes apart from mode 6 which is an Antarctic teleconnection pattern and mode 8 which is a SH blocking mode. In contrast, for 1975–1994, as shown in Table 2, the first 20 modes include a greater variety, because of the drop in growth rates of the SH cyclogenesis modes, including also SH blocking and northwest cloud band disturbances.

6. Structures of southern hemisphere cyclogenesis modes

Next we examine the structures of the leading SH cyclogenesis modes during the two periods of interest. Figure 7 shows the

Table 1. Periods T_r^d, growth rates ω_i^d and e-folding times τ_i^d, of the 20 fastest growing modes for the 1949–1968 NCEP/NCAR basic state with standard parametrizations ($K'^d = 2.338 \times 10^{16}$ m^4 s^{-1}, $Q_F^d = 1500$ K,$C_F^d = 5 \times 10^{-4}$ Km^{-1}), their mode number and class of mode. Also shown are the largest pattern correlations A_c between a given mode and the modes for the 1975–1994 NCEP/NCAR basic state with standard parametrizations and the 1975–1994 mode for which the pattern correlation is largest. The modes are classified as southern hemisphere monopole cyclogenesis (shC), northern hemisphere monopole cyclogenesis (nhC), southern hemisphere dipole cyclogenesis (shDC), southern hemisphere blocking (shB), Antarctic teleconnection pattern (aTP), northern hemisphere tropical wave (nhTW) and southern hemisphere northwest cloud band (shNWCB)

Class	Mode 1949–1968	T_r^d (d)	ω_i^d (d^{-1})	τ_i^d (d)	A_c	Mode 1975–1994
shC	1	1.20	0.4250	2.353	0.9148	9
nhC	2	2.77	0.4006	2.500	0.9340	1
shC	3	0.98	0.3930	2.544	0.9564	20
shC	4	2.29	0.3768	2.654	0.7566	15
shC	5	2.64	0.3678	2.719	0.7655	13
aTP	6	13.08	0.3624	2.759	0.9416	3
nhC	7	3.57	0.3497	2.860	0.9474	2
shB	8	7.40	0.3495	2.861	0.8342	4
shDC	9	2.99	0.3328	3.005	0.5733	31
shC	10	3.10	0.3308	3.023	0.7255	19
shDC	11	5.22	0.3184	3.141	0.8468	6
shC	12	2.01	0.3182	3.142	0.5676	25
shDC	13	3.50	0.3176	3.149	0.5631	19
nhC	14	3.20	0.3100	3.226	0.8613	5
shDC	15	2.57	0.3095	3.231	0.5385	16
shC&nhC	16	3.75	0.3007	3.326	0.5531	27
shDC	17	2.36	0.2948	3.392	0.3998	25
shC	18	1.99	0.2942	3.398	0.6345	61
shC	19	1.77	0.2926	3.417	0.6324	61
shDC&nhC	20	4.13	0.2925	3.419	0.5659	8

Table 2. As in Table 1 but for modes growing on the 1975–1994 basic state (and with the roles of the two basic states interchanged)

Class	Mode 1975–1994	T_r^d (d)	ω_i^d (d^{-1})	τ_i^d (d)	A_c	Mode 1949–1968
nhC	1	2.64	0.4160	2.404	0.9340	2
nhC	2	3.50	0.3696	2.706	0.9474	7
aTP	3	17.48	0.3606	2.773	0.9416	6
shB	4	8.02	0.3317	3.015	0.8342	8
nhC	5	3.13	0.3212	3.113	0.8613	14
shDC	6	5.08	0.3101	3.225	0.8468	11
nhTW	7	3.83	0.3071	3.256	0.7959	22
shDC&nhC	8	3.86	0.2829	3.535	0.5659	20
shC	9	1.30	0.2824	3.541	0.9148	1
nhC	10	4.10	0.2768	3.613	0.8316	33
aTP	11	21.26	0.2700	3.703	0.8524	26
shNWCB	12	8.19	0.2624	3.812	0.8036	43
shC	13	2.83	0.2583	3.871	0.7655	5
nhC	14	4.95	0.2578	3.879	0.5734	46
shC	15	2.51	0.2535	3.944	0.7566	4
shDC	16	2.39	0.2440	4.098	0.5385	15
shC&nhC	17	5.96	0.2391	4.180	0.8629	42
shDC	18	2.06	0.2392	4.181	0.5319	28
shC	19	3.31	0.2342	4.270	0.7255	10
shC	20	1.03	0.2288	4.370	0.9564	3

upper level streamfunction, lower level streamfunction and upper level divergence of mode 1 for the 1949–1968 basic state (at a particular phase or time) and as well the random phase ensemble average (RPEA) of these quantities defined as in eq. (2.7) of Frederiksen (1982). The RPEA of a disturbance field is essentially the amplitude envelope within which the disturbance propagates with changing time or phase and determines in this case the structure of the storm track. We note from Figs. 7a–c that the disturbance has a wavenumber of around 12 in the regions of large amplitude over southern Australia and consists of a series of eastward propagating troughs (lighter shading) and ridges (darker shading). As the troughs and ridges move eastward they amplify to reach a maximum in preferred regions of large RPEA amplitude. In Figs. 7d–f the amplitude variations of the storm mode are more evident with all the fields shown having largest amplitude focused over southwestern Australia and secondary maxima over the central Southern Pacific Ocean. From the Appendix, we note that the precipitation (A.4) due to convection is essentially determined by the lower level vertical velocity in pressure coordinates and in our model this is proportional to the magnitude of the upper-level divergence. Thus, the pattern of RPEA divergence in Fig. 7f is also the expected pattern of rainfall associated with this mode, and as we have noted above the maximum is focused over southwestern Australia.

Mode 1, shown in Fig. 7, is the fastest growing of a class of cyclogenesis modes with zonal wavenumbers between 6 and 12 and large amplitudes in the Australian region. For example, mode 4 (not shown) has a zonal wavenumber of $m \sim 8$ and mode 5 (not shown) of around $m \sim 6$. Of course, as cyclogenesis modes grow and non-linear effects become more important their dominant wavenumbers tend to decrease resulting in larger scale mature disturbances (Frederiksen, 1981a, b and c). Figure 3a of Qi et al. (1999) shows the scale of a typical low in the southern Australian region that is consistent with our results. We note that there are also cyclogenesis modes such as mode 9 (not shown) that grow on the polar front jet and has large amplitudes near 50S, similar to the mode shown in Fig. 5 of Frederiksen and Frederiksen (1993b); note also the discussion in Section 1.

For the 1975–1994 basic state, mode 1 in Table 2 is a northern hemisphere storm track mode (not shown) with largest amplitudes in streamfunction fields over the central Northern Pacific Ocean near 170°E and 45°N. The leading SH cyclogenesis mode for this 1975–1994 basic state is mode 8, which as noted in Section 5 has a growth rate that is around 30% less than for mode 1 for the 1949–1968 basic state. Figure 8 shows the same fields as in Fig. 7 but for mode 8 for the 1975–1994 basic state. We note from Figs. 8a–c that the upper and lower level disturbance streamfunctions and upper-level divergence have quite different structures to mode 1 for the 1949–1968 basic state. Mode 8 for the 1975–1994 basic state effectively bypasses southwestern Australia and has maximum impact over the central Southern Pacific Ocean. These findings are perhaps most evident in the RPEA of these fields shown in Figs. 8d–f that exhibit primary maxima of the storm tracks near 120°W and between 30° and 40°S. We also note that mode 8 has longer period and somewhat larger scale structure than mode 1 for the 1949–1968 basic state. In fact, as seen from Table 2, mode 8 for the 1975–1994

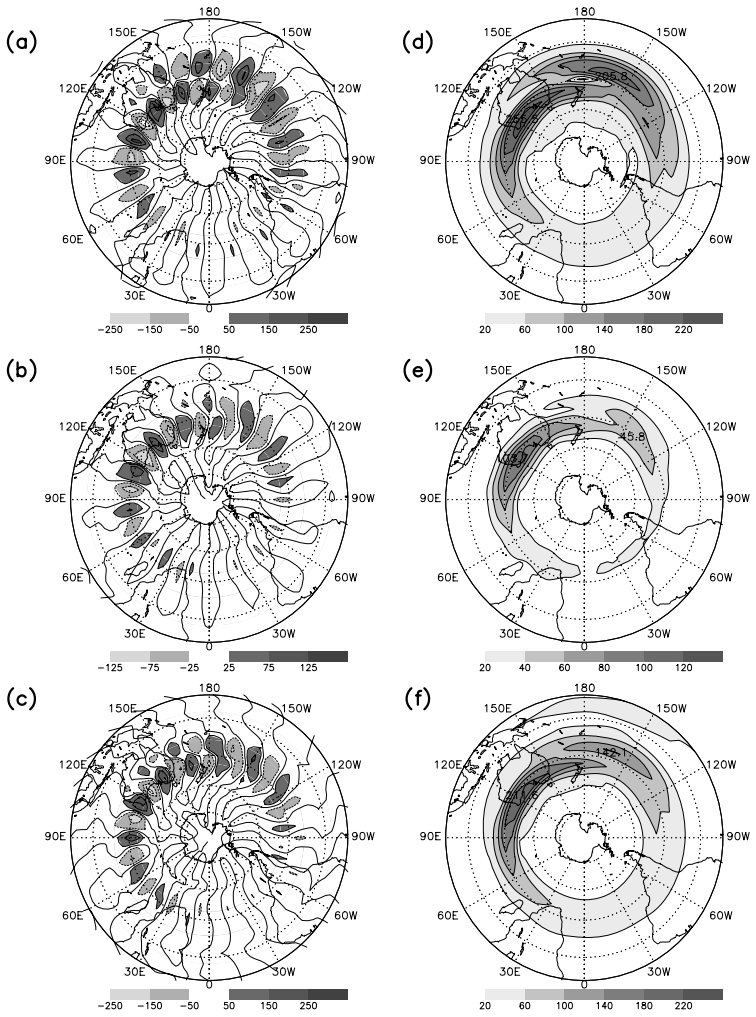

Fig. 7. Shown in arbitrary units are (a) the upper-level streamfunction $\left(\psi^1\right)$, (b) the lower-level streamfunction $\left(\psi^3\right)$ and (c) the upper-level divergence $(-D)$ for the fastest growing SH cyclogenesis mode, mode 1, for the July 1949–1968 basic state with standard parametrizations and the corresponding RPEA of (d) the upper-level streamfunction $\left(\psi^1\right)$, (e) the lower-level streamfunction $\left(\psi^3\right)$ and (f) the upper-level divergence $(-D)$. Contour intervals are 100, 50, 100, 40, 20 and 40, respectively and the divergence has been scaled by 10^{-2}.

basic state is most similar to mode 20 for the 1949–1968 basic state, with a pattern correlation of 0.5659; for these modes that largely miss Australia there is negligible differences in their growth rates.

There are, however, other subdominant weather modes for the 1975–1994 basic state, with a similar structure and period to mode 1 for the earlier stage. Mode 9 for the later basic state is the fastest growing of this group of modes and also has the largest pattern correlation (0.9148) with mode 1 for the earlier stage as shown in Table 1. Figure 9 again shows the same disturbance fields as in Fig. 7 but for mode 9 for the 1975–1994 basic state. It is clear that the modal structures shown in Fig. 9 are quite similar to those in Fig. 7, as quantified by the pattern correlation that is larger than 0.9. However, as noted in Section 5, the growth rate for mode 9 for the 1975–1994 basic state is around 30% less than for mode 1 for the earlier stage and this is consistent with the observed reduction in rainfall over southern Australia, and in particular, SWWA. We also note that in the later time period the impact of the cyclogenesis has shifted slightly downstream or eastward [25° in longitude from (35°S, 125°E) to (35°S, 150°E)] as seen particularly by comparing the RPEA upper-level streamfunction fields in Figs. 7d and 9d.

The weather modes in Figs. 7–9 extend around much of the hemisphere, in common with leading cyclogenesis modes, growing on climatological basic states, which capture the geographical structure of the observed storm tracks (Frederiksen, 1985, 1992; Frederiksen and Frederiksen, 1993b; Hall and Sardeshmukh, 1998). Cyclogenesis modes growing on instantaneous basic states may be more localized because of the sharper gradients in baroclinicity, as in fig. 8a of Frederiksen and Bell (1990). In nature, individual storms tend to develop just downstream and slightly poleward of the maximum baroclinicity that may be quite localized, as discussed in Section 1. Frequently, downstream baroclinic development occurs resulting in a wavetrain along the major storm tracks (Danielson et al., 2004, and references therein). Since climatological basic states are averages of many instantaneous flow fields the local variations in baroclinicity are generally less than for instantaneous basic states. As a consequence the modes growing on climatological basic states represent average instability properties and tend to

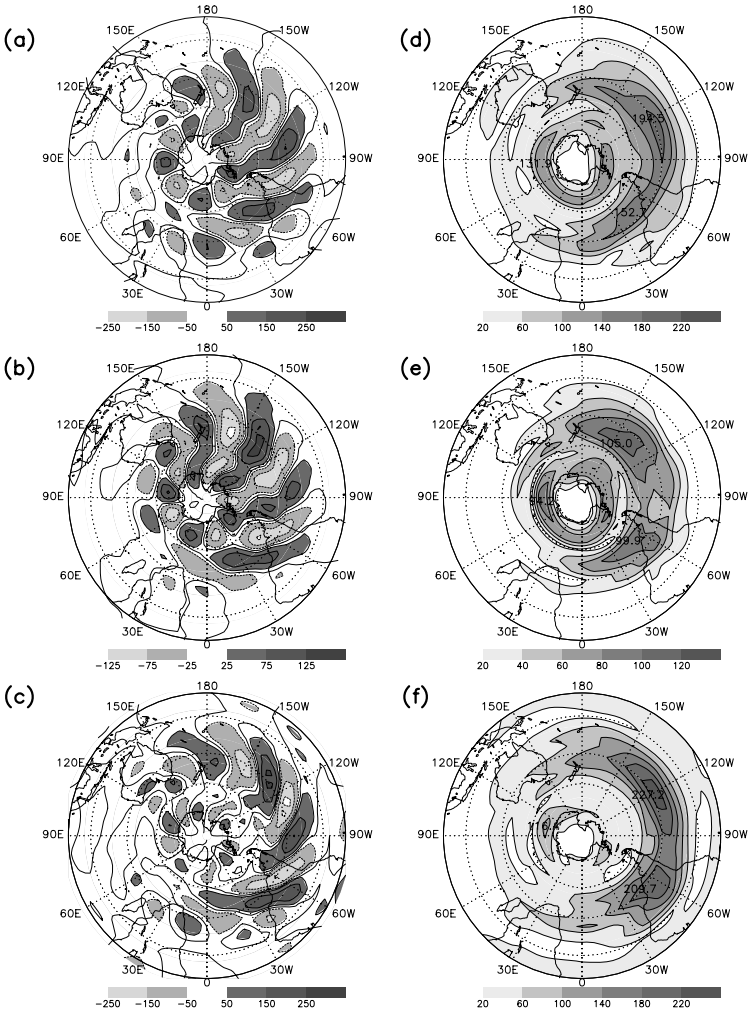

Fig. 8. As in Fig. 7 but for the fastest growing SH cyclogenesis mode, mode 8, for the July 1975–1994 basic state and the divergence scaled by 5×10^{-2}.

capture the central regions of the observed storm tracks rather than representing individual cyclones, as discussed in more detail by Frederiksen (1992). Pierrehumbert and Swanson (1995) also note that absolute instability leading to local modes is in general not a prominent mechanism for typical climatological basic states, particularly with jets that are everywhere westerly. They discuss the possibility that undisturbed baroclinic zones act as amplifiers for baroclinic debris entering from upstream in a continuous series of life cycles around the hemisphere and see synoptic eddies as wave packet of growing normal modes modified as they progress through the non-linear life cycle.

The general properties of the storm modes outlined above are also characteristic of many of the other SH cyclogenesis modes listed in Tables 1 and 2. Similar modes crossing the Australian region, but with somewhat larger scales, include mode 4 ($m \sim 8$) and mode 5 ($m \sim 6$) for the 1949–1968 basic state and modes 15 ($m \sim 8$) and 13 ($m \sim 6$) for the 1975–1994 basic state, that have 33 and 30% smaller growth rates than for the earlier period, respectively. Importantly, as detailed in Section 5, the 10 leading SH cyclogenesis modes for 1975–1994 have growth rates that are on average 32% smaller than for the corresponding modes for 1949–1968 and this reduction is particularly notable for storm modes crossing southern Australia.

These results again suggest that a primary cause of the rainfall reduction over SWWA in the period 1975–1994 is the reduction in the intensity of cyclogenesis due to a reduction in the baroclinic instability of the large-scale SH circulation. There are also some changes in other mode types between the two periods but they are less important and will not be detailed here.

7. Sensitivity studies

7.1. Sensitivity to parameter specifications

Next, we examine the sensitivity of our results to the strengths of the dissipation, convection and evaporation feedback parametrizations. We have repeated the instability calculations in Sections 5 and 6 for the following five sets of three parameters (K'^d, Q_F^d, C_F^d): ($2.338 \times 10^{16}\,\mathrm{m^4\ s^{-1}}$, 1000 K, $5 \times 10^{-4}\,\mathrm{Km^{-1}}$), ($2.338 \times 10^{16}\,\mathrm{m^4\ s^{-1}}$, 1000 K, $0\,\mathrm{Km^{-1}}$), ($2.338 \times 10^{16}\,\mathrm{m^4\ s^{-1}}$,

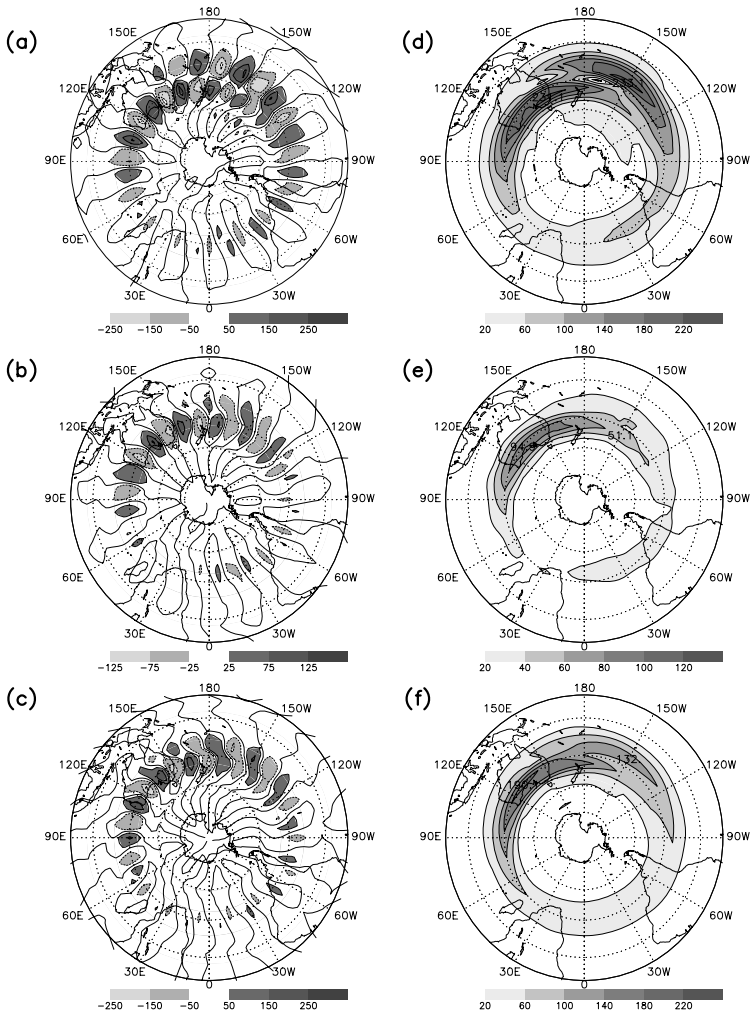

Fig. 9. As in Fig. 7 but for the second fastest growing SH cyclogenesis mode, mode 9, for the July 1975–1994 basic state.

Table 3. Periods T_r^d, growth rates ω_i^d and e-folding times τ_i^d, of modes for the 1949–1968 basic state with different K'^d, Q_F^d and C_F^d that have the largest pattern correlations A_c with mode 1 for the 1949–1968 basic state with standard parametrizations. Also shown are the mode numbers

Mode	1949–1968 basic states							
	K'^d ($m^4 s^{-1}$)	Q_F^d (K)	C_F^d (Km^{-1})	T_r^d (d)	ω_i^d (d^{-1})	τ_i^d (d)	A_c	Mode
1	2.338×10^{16}	1000	5×10^{-4}	1.194	0.3861	2.590	0.9959	1
2	2.338×10^{16}	1000	0	0.975	0.3825	2.614	0.9955	1
3	2.338×10^{16}	0	0	1.179	0.3246	3.081	0.9869	1
2	0	1500	5×10^{-4}	1.196	0.7030	1.422	0.9784	1
17	4.676×10^{16}	1500	5×10^{-4}	1.199	0.2172	0.2172	0.9719	1

0 K, 0 Km^{-1}), (0 m^4 s^{-1}, 1500 K, 5×10^{-4} Km^{-1}) and (4.676×10^{16} m^4 s^{-1}, 1500 K, 5×10^{-4} Km^{-1}). Table 3 shows the periods T_r^d, growth rates ω_i^d, and e-folding times τ_i^d, of the modes for the 1949–1968 basic state with different K'^d, Q_F^d and C_F^d that have the largest pattern correlations A_c with mode 1 (growth rate of 0.4250 d^{-1}) for the 1949–1968 basic state with the standard parametrizations ($K'^d = 2.338 \times 10^{16}$ m^4 s^{-1}, $Q_F^d = 1500$ K, $C_F^d = 5 \times 10^{-4}$ Km^{-1}). We note from Tables 1 and 3 that weaker convection results in a drop in the growth rates as expected while surface evaporation has less effect on these baroclinic eddies. We also observe that whether the mode shown in Fig. 7 is the fastest growing or is a subdominant mode depends to some extent on the strengths of the dissipation and moisture parametrizations. In all cases the storm track modes in Table 3 have pattern correlations A_c that are close to unity reflecting the very close similarity in the structures of the modes.

Table 4. As in Table 3 for modes for 1975–1994 basic states that have the largest pattern correlations A_c with mode 9 for the 1975–1994 basic state with standard parametrizations

	1975–1994 basic states							
Mode	K'^d ($m^4\ s^{-1}$)	Q_F^d (K)	C_F^d (Km^{-1})	T_r^d (d)	ω_i^d (d^{-1})	τ_i^d (d)	A_c	Mode
7	2.338×10^{16}	1000	5×10^{-4}	1.293	0.2488	4.019	0.9942	9
6	2.338×10^{16}	1000	0	1.289	0.2617	3.822	0.9927	9
6	2.338×10^{16}	0	0	1.279	0.1989	5.027	0.9760	9
5	0	1500	5×10^{-4}	1.283	0.5218	1.916	0.9671	9
49	4.676×10^{16}	1500	5×10^{-4}	1.312	0.0820	12.20	0.9635	9

Table 5. As in Table 3 for modes, growing on either NCEP/NCAR or ERA-40 basic states with standard parametrizations, that have largest pattern correlations A_c, with mode 1 for the 1949–1968 basic state

Basic state	Mode	T_r^d (d)	ω_i^d (d^{-1})	τ_i^d (d)	A_c	Mode
1963–1968 NCEP/NCAR	2	1.185	0.4410	2.267	0.9683	1
1963–1968 ERA-40	3	1.179	0.4312	2.319	0.8836	1
1959–1968 NCEP/NCAR	2	1.207	0.4095	2.442	0.9929	1
1959–1968 ERA-40	3	1.213	0.4228	2.365	0.9031	1

Table 6. As in Table 5 for modes that have largest pattern correlations A_c with mode 9 for the 1975–1994 basic state

Basic state	Mode	T_r^d (d)	ω_i^d (d^{-1})	τ_i^d (d)	A_c	Mode
1975–1980 NCEP/NCAR	2	1.294	0.3671	2.724	0.9584	9
1975–1980 ERA-40	4	1.256	0.3694	2.707	0.9685	9
1975–1984 NCEP/NCAR	5	1.319	0.3094	3.232	0.9815	9
1975–1984 ERA-40	6	1.297	0.3236	3.091	0.9761	9

Table 4 shows the corresponding results for 1975–1994 basic state modes that are closely related to the storm track mode 9 in Fig. 9 (growth rate of 0.3861 d^{-1}) for the 1975–1994 basic state with the standard parametrizations. Again, mode numbers depend to some extent on the dissipation and moisture parametrizations and growth rates increase with the strength of the convection while there is very little change in the structures of the modes. In all cases growth rates of the modes in Table 4 are considerably smaller than for the corresponding modes in the Table 3 with a reduction ranging from 26 to 62% (see Table 8).

7.2. Sensitivity to basic states

As noted in Section 3, we recognize that reanalysed data may have some limitations in accuracy (Hines et al., 2000; Simmons et al., 2004). For this reason, we also examine how our results depend on whether the NCEP/NCAR data set or the ERA-40 data set is used. The ERA-40 data set is not available back to 1949 and for this reason we focus on comparisons for 1959–1968 versus 1975–1984 and 1963–1968 versus 1975–1980 for both data sets. As well we compare results for these data sets with the NCEP/NCAR data for the longer 20-yr periods that have formed the basis of our studies in the previous sections.

Table 5 shows the periods T_r^d, growth rates ω_i^d and e-folding times τ_i^d, of the modes for averaged basic states ending in 1968, and with standard parametrizations, that have largest pattern correlations with mode 1 for the 1949–1968 basic state. The pattern correlations are generally close to or greater than 0.9 and the growth rates vary by less than 10%. Similar results are shown in Table 6 for modes growing on averaged basic states starting in 1975 and that have largest pattern correlations with mode 9 for the 1975–1994 basic state. The pattern correlations are close to or greater than 0.96 and growth rates vary by less than 20%.

Some of the differences in modal properties in Tables 5 and 6 are of course due to the different number of years in the averaging periods. The roles of just the data sources may be seen in Table 7. There the pattern correlations of the SH storm track modes (in Tables 5 and 6) for ERA-40 and NCEP/NCAR data for the same periods are listed and the percentage changes in growth rates noted. We see that pattern correlations are greater than or close to 0.94 and growth rates vary by around 4% or less.

Table 7. Pattern correlations A_c between leading SH storm track modes for ERA-40 and NCEP/NCAR basic states with standard parametrizations, their mode numbers and the percentage growth rate reduction with the NCEP/NCAR data set compared with the ERA-40 data set

Basic state	Mode	Basic state	Mode	A_c	Growth rate reduction (%)
1963–1968 ERA-40	3	1963–1968 NCEP/NCAR	2	0.9396	−2
1975—1980 ERA-40	4	1975–1980 NCEP/NCAR	2	0.9685	+0.6
1959–1968 ERA-40	3	1959–1968 NCEP/NCAR	2	0.9583	+3
1975–1984 ERA-40	6	1975–1984 NCEP/NCAR	5	0.9872	+4.4

Table 8. As in Table 7 for basic states with dissipation parameters as shown, and otherwise standard parametrizations, and showing the percentage growth rate reduction for modes on basic states starting in 1975 compared with those on basic states ending in 1968

K'^d ($m^4 s^{-1}$)	Basic state	Mode	Basic state	Mode	Growth rate reduction (%)
2.338×10^{16}	1949–1968 NCEP/NCAR	1	1975–1994 NCEP/NCAR	9	33.5
0	1949–1968 NCEP/NCAR	2	1975–1994 NCEP/NCAR	5	25.8
4.676×10^{16}	1949–1968 NCEP/NCAR	17	1975–1994 NCEP/NCAR	49	62.2
2.338×10^{16}	1963–1968 NCEP/NCAR	2	1975–1980 NCEP/NCAR	2	16.8
2.338×10^{16}	1963–1968 ERA-40	3	1975–1980 ERA-40	4	14.3
2.338×10^{16}	1959–1968 NCEP/NCAR	2	1975–1984 NCEP/NCAR	5	24.4
2.338×10^{16}	1959–1968 ERA-40	3	1975–1984 ERA-40	6	23.5

Finally, in Table 8 we list the percentage changes in the growth rates of SH storm track modes before and after the early 1970s for different averaging periods and strengths of the dissipation parametrization. The modes considered are those with largest pattern correlations with mode 1 for the 1949–1968 basic state or mode 9 for the 1975–1994 basic state (as in Tables 3–7). For the 20-yr averaged basic states the smallest reduction in growth rate in the latter period is about 26% and occurs for zero dissipation. For the standard parametrization cases the smallest reduction in growth rate is circa 14% and occurs for the 6-yr averaged ERA-40 basic state for 1975–1980. For the 10-yr averaged basic states for both ERA-40 and NCEP/NCAR the growth rate reduction is about 24% for 1975–1984. For the longer 20-yr averaged basic states the growth rate reduction is 33.5%. It is noteworthy that the growth rate reduction increases with increasingly longer averaging periods and is least for the 6 yr averages on either side of the early 1970s shift in the large-scale circulation.

8. Discussion and conclusions

The aim of this paper has been to examine the interdecadal changes in the instability properties of the SH winter large-scale flow, before and after the early to mid-1970s, and the associated changes in the structures and growth rates of leading SH cyclogenesis modes. Our study has been motivated by the dramatic reduction in average winter rainfall in the SWWA that occurred after the mid-1970s. We have noted that in the period 1975–1994 there has been a reduction of about 9 m s^{-1} in the strength of the July peak subtropical zonal wind, near 30°S and at the 200 hPa pressure level, compared with the period 1949–1968. This has been related to a significant warming of the SH troposphere south of 30°S, resulting in a reduction of the equator-to-pole temperature gradient in the latter period. There have also been significant changes in both the Hadley and Walker circulations. Changes in the dry and moist static stability and in surface evaporation in contrast appear to be less significant.

We have examined the associated changes between the two periods in the Phillips (1954) criteria for baroclinic instability, for both dry and moist static stability and generalized for spherical geometry as used in FF93a, b. In the SH mid-latitudes these instability criteria for storm generation reflect closely the strength of the upper tropospheric zonal winds. Both dry and moist differences in the criteria show a reduction in the likely cyclogenesis after the mid-1970s in a band around 30°S and stretching longitudinally across most of the SH including SWWA. As well there are bands of increased likelihood of cyclogenesis at southern latitudes of the SH, particularly between Australia and Antarctica and in the Northern Hemisphere Asian and Pacific storm tracks.

A particular focus of our work has been to perform detailed examinations of the interdecadal changes in SH winter cyclogenesis using the global two-level primitive equation instability model with the 1949–1968 and 1975–1994 NCEP/NCAR reanalysed observed July basic states. Our study has also included the effects of topography, convection, evaporation and dissipation. The convection has been specified through a generalized Kuo-type parametrization and the evaporation through a bulk aerodynamic formula. We have examined the growth rates, e-folding times, periods and structures of dominant cyclogenesis modes based on the primitive equation instability calculations.

For the 1949–1968 basic state (with our standard parametrizations of dissipation and moisture) the fastest growing mode is a SH cyclogenesis mode consisting of a series of eastward

propagation troughs and ridges, and with zonal wavenumber of $m \sim 12$, in the regions of large amplitude over southern Australia. Peak amplitudes of streamfunctions and divergence, and therefore rainfall, are located over and near SWWA. In contrast for the corresponding 1975–1994 basic state the fastest growing mode is a NH cyclogenesis mode with maximum amplitude in the Northern Pacific storm track and the first mode corresponding to SH cyclogenesis is the eighth fastest growing disturbance, mode 8. This mode has a growth rate that is about 30% less than for mode 1 for the 1949–1968 basic state, is of larger scale, and moreover effectively bypasses southwestern Australia and instead has maximum impact over the central Southern Pacific Ocean. The second mode corresponding to SH cyclogenesis in the latter period is mode 9 and it is much more similar to mode 1 for the 1949–1968 basic state, with pattern correlation around 0.9. Mode 9 for the latter stage however has a growth rate that is 33% less than that for mode 1 for the earlier time period and the impact of the cyclogenesis has shifted slightly eastward [25° in longitude from (35°S, 125°E) to (35°S, 150°E)].

We have also found that the general properties of the few leading SH storm modes discussed above are characteristic of many of the other SH cyclogenesis modes including modes with $m \sim 6$. In particular, the 10 leading SH cyclogenesis modes for 1975–1994 have on average growth rates that are 32% smaller than for the corresponding modes for 1949–1968. Further, this reduction in the latter period primarily applies to cyclogenesis modes crossing southern Australia.

We have performed extensive studies of the sensitivity of our results to the strengths of the dissipation, convection and evaporation parameters, on whether the NCEP/NCAR or ERA-40 data sets are employed, and to the number of years in the averaging periods defining the basic states. We find remarkable consistency in the structures of the leading storm track modes crossing Australia in these sensitivity studies. We also find that the growth rates of the leading SH cyclogenesis modes vary at most by 4.4% between the NCEP/NCAR and ERA-40 data sets averaged over the same years. The growth rate reduction of leading storm track modes across Australia, in the period after the mid-1970s, increases with increasingly longer averaging periods. With our standard specification of the physical parametrizations, the growth rate reduction is as low as 14% for 6 yr averages, increases to about 24% for 10 yr averages and to 33% for 20 yr averages. With no bi-harmonic dissipation, the growth rate reduction in the latter 20 yr period is as low as 26% and increases with the strength of the dissipation. We have found that our general conclusions, on the growth rate reduction of leading SH storm track modes in the period after the mid-1970s, are relatively insensitive to the strengths of the convection and surface evaporation examined.

As noted in Section 1, a number of observational studies have demonstrated strong correlations between deepening rates of storms and precipitation. There may be other contributing causes to the observed rainfall reduction over SWWA since the mid-1970s such as changes to the land surface and associated fluxes due to land clearing (IOCI, 2002). However, the reduction in the intensity of cyclogenesis and the related changes in the instability properties of the large scale SH circulation are so dramatic that we conclude that they are the primary cause of the rainfall reduction.

While the observed changes in the SH climate, including the reduction in the equator-to-pole tropospheric temperature gradient and consequent zonal flow reduction in the latter period, are not inconsistent with climate change due to anthropogenic forcing from increasing greenhouse gases, this has not at this stage been established. However, on the basis of the modelling studies of Fyfe (2003) and Brandefelt and Källén (2004), and the general principles discussed here, one might expect a reduction in both cyclogenesis over southern Australia and in SH mid-latitude mature storm activity due to increased anthropogenic greenhouse forcing. We hope in future studies to examine this and other possible causes for the large changes in the SH large-scale circulation and transient instabilities that have occurred since the mid-1970s.

9. Acknowledgments

It is a pleasure to thank Steve Kepert, Stacey Osbrough and Janice Sissons for assistance with this work. This work was partly funded by the Indian Ocean Climate Initiative of the W.A. Department of Environment, Water and Catchment Protection and the Australian Greenhouse Office, and contributes to the research effort of the CSIRO Water for Healthy Country Flagship.

10. Appendix: generalized Kuo convective parametrization

In pressure coordinates, the large-scale equations for potential temperature Θ and specific humidity q are (Molinari 1985)

$$\frac{\partial \Theta}{\partial t} + \nabla \cdot (v\Theta) + \frac{\partial}{\partial p}(w\Theta) = \left(\frac{p_{1000}}{p}\right)^{\kappa} \frac{Q(p)}{c_p} \tag{A.1}$$

$$\frac{\partial q}{\partial t} + \nabla \cdot (\mathbf{v}q) + \frac{\partial}{\partial p}(wq) = -C^* + g\frac{\partial F_q}{\partial p} \tag{A.2}$$

with

$$Q(p) = LC^*. \tag{A.3}$$

Here, $\kappa = R/c_p$, $c_p = 1004$ JK^{-1} kg^{-1} is the specific heat of air at constant pressure, $R = 287$ K^{-1} kg^{-1} is the gas constant for air, $L = 2.5 \times 10^6$ J kg^{-1} is the latent heat of condensation, $g = 9.8$ m s^{-2} is the gravitational acceleration, $p_{1000} = 1000$ hPa, p is pressure, $\mathbf{v}$ is the vector horizontal wind, $w = \mathrm{d}p/\mathrm{d}t$ is the vertical velocity in pressure coordinates and $Q(p)$ is the heating rate. Also, C^* is the condensation minus evaporation rate, F_q represents the boundary-layer turbulent flux of moisture

and for this study we shall ignore the radiative heating rate and boundary-layer turbulent fluxes of heat.

The rate of precipitation P reaching the surface of the atmosphere is

$$P = \frac{1}{g}\int_o^{p_{1000}} \mathrm{d}p\, C^*. \tag{A.4}$$

Kuo (1974) assumed that a proportion $(1 - b)$ of the total convergence of moisture, or 'moisture accession', M_t, is condensed and precipitated out as rain or carried away and the fraction b increases the humidity of the air. Here

$$M_t = -\frac{1}{g}\int_o^{p_{1000}} \mathrm{d}p \nabla \cdot (\mathbf{v}q) + E, \tag{A.5}$$

where the surface evaporation rate is

$$E = F_q\,(p_{1000})\,. \tag{A.6a}$$

The surface evaporation is parametrized by the bulk aerodynamic form

$$E = C_E \rho\,(p_{1000})\,|\mathbf{v}(p^*)|\,[q_s(p_{1000}) - q(p^*)], \tag{A.6b}$$

where p^* is a level closest to the surface, C_E is a non-dimensional drag coefficient and $\rho\,(p_{1000}) = 1.276\,\mathrm{kg\,m^{-3}}$ is the surface density of air.

In this paper, we shall follow modifications to the Kuo scheme proposed by Kanamitsu (1975) and Krishnamurty et al. (1976). They wrote the moisture accession in the approximate form

$$M_t = -\frac{1}{g}\int_o^{p_{1000}} \mathrm{d}p\, w\frac{\partial q}{\partial p} + E \tag{A.7}$$

obtained from the continuity equation and assuming that q is slowly varying. Further, we follow Molinari (1985) and replace Kuo's relaxation of the potential temperature towards a moist adiabat by a prescribed heating profile and introduce a similar profile of moistening into the moisture equation. Thus,

$$Q(p) = gL(1 - b)M_t\eta(p) \tag{A.8}$$

and

$$\frac{\partial q}{\partial t} + \nabla \cdot (\mathbf{v}q) + \frac{\partial}{\partial p}\,(wq) = -g(1 - b)M_t\eta_q(p). \tag{A.9}$$

The normalized heating profile $\eta(p)$ satisfies

$$\int_o^{p_{1000}} \mathrm{d}p\,\eta(p) = 1 \tag{A.10}$$

and the moistening profile $\eta_q(p)$ is similarly normalized.

For the two-level model, $|w|$ increases linearly from $|w_0| = |w\,(p_0)| = 0$ to $|w_2| = |w\,(p_{500})|$ with increasing p and decreases linearly from $|w_2|$ to $|w_4| = |w\,(p_{1000})|$ with p. Also, for simplicity we assume that $q = 0$ for $p \le p_{500}$ and q increases linearly with p to $q\,(p_{1000})$; the condensation level is taken to be $p_{750} =$ 750 hPa. The pressure spacing is $\Delta p = 250$ hPa. The moisture accession then becomes

$$M_t = \frac{-2w(p_{750})q(p_{750})}{g} + E \tag{A.11}$$

and the heating entering the vertical mean (θ) and shear (σ) potential temperature equations is given by (FF93a)

$$\tilde{Q}_\theta = \frac{1}{2}\left[\tilde{Q}_\Theta\,(p_{250}) + \tilde{Q}_\Theta\,(p_{750})\right], \tag{A.12a}$$

$$\tilde{Q}_\sigma = \frac{1}{2}\left[\tilde{Q}_\Theta\,(p_{250}) - \tilde{Q}_\Theta\,(p_{750})\right] \tag{A.12a}$$

with

$$\tilde{Q}_\theta = \left(\frac{p_{1000}}{p}\right)^\kappa \frac{Q(p)}{c_p}. \tag{A.13}$$

As in FF93a, the heating profile is chosen such that the heating projects completely onto the internal mode; that is, $\tilde{Q}_\sigma$ vanishes. Also proceeding as in appendix A of FF93a we find that

$$\tilde{Q}_\theta = -\frac{Q_F}{\Delta p}q(p_{750})w(p_{750}) + C_F\,|\mathbf{v}(p^*)|\,[q_s(p_{1000}) - q(p^*)], \tag{A.14}$$

where

$$Q_F = \frac{2(1 - b)A_F L}{c_p} = \frac{mA_F L}{c_p}, \tag{A.15}$$

$$C_F = \frac{C_E\rho(p_{1000})g(1 - b)A_F L}{\Delta p\, c_p}. \tag{A.16}$$

Also, $m = 2(1 - b)$ is the moisture availability factor and

$$A_F = \left[\left(\frac{p_{750}}{p_{1000}}\right)^\kappa + \left(\frac{p_{500}}{p_{1000}}\right)^\kappa + \left(\frac{p_{250}}{p_{1000}}\right)^\kappa\right]^{-1}. \\ = 0.414. \tag{A.17}$$

Now, the linearized expression for $\tilde{Q}_\theta$ given in eq. (1) is obtained by approximating the velocity at p^* by one half the value at 750 hPa and q_s at 1000 hPa and q at p^* by twice their values at 750 hPa. Note also that the 750-hPa divergence is just $\Delta\, p$ times the 750-hPa vertical velocity.

References

Allan, R. J. and Haylock, M. R. 1993. Circulation features associated with the winter rainfall decrease in south-western Australia. *J. Climate* **6**, 1356–1367.

Anderson, J. L. 1991. The robustness of barotropic unstable modes in a zonally varying atmosphere. *J. Atmos. Sci.* **48**, 2393–2410.

Arblaster, J. M., Meehl, G. A. and Moore, A. M. 2002. Interdecadal modulation of Australian rainfall. *Clim. Dyn.* **18**, 519–531.

Brandefelt, J. and Källén, E. 2004. The response of the Southern Hemisphere atmospheric circulation to an enhanced greenhouse gas forcing. *J. Climate* **17**, 4425–4442.

Branstator, G. 1985. Analysis of general circulation model sea-surface temperature anomaly simulations using a linear model. Part II: eigenanalysis. *J. Atmos. Sci.* **42**, 2241–2254.

Branstator, G. and Held, I. 1995. Westward propagating normal modes in the presence of stationary background waves. *J. Atmos. Sci.* **44**, 247–262.

Cai, W., Whetton, P. H. and Karoly, D. J. 2003. The response of the Antarctic Oscillation to increasing and stabilized atmospheric CO2. *J. Climate* **16**, 1525–1538.

Danielson, R. E., Gyakum, J. R. and Straub, D. N. 2004. Downstream baroclinic development among forty-one cold-season eastern North Pacific cyclones. *Atmos. Ocean* **42**, 235–250.

Drosdowsky, W. 1993. Potential predictability of winter rainfall over southern and eastern Australia using Indian Ocean sea-surface temperature anomalies. *Aust. Met. Mag.* **42**, 1–6.

Frederiksen, C. S. and Frederiksen, J. S. 1992. Northern Hemisphere storm tracks and teleconnection patterns in primitive equation and quasi-geostrophic models. *J. Atmos Sci.* **49**, 1443–1458.

Frederiksen, C. S. and Frederiksen, J. S. 1996. A theoretical model of northwest cloudband disturbances and southern hemisphere storm tracks: the role of SST anomalies. *J. Atmos. Sci.* **53**, 1410–1432.

Frederiksen, J. S. 1981a. Disturbances and eddy fluxes in Southern Hemisphere flows: linear theory. *J. Atmos. Sci.* **38**, 673–689.

Frederiksen, J. S. 1981b. Growth and vacillation cycles of disturbances in Southern Hemisphere flows. *J. Atmos. Sci.* **38**, 1360–1375.

Frederiksen, J. S. 1981c. Scale selection and energy spectra of disturbances in Southern Hemisphere flows. *J. Atmos. Sci.* **38**, 2573–2584.

Frederiksen, J. S. 1982. A unified three-dimensional instability theory of the onset of blocking and cyclogenesis. *J. Atmos. Sci.* **39**, 969–987.

Frederiksen, J. S. 1983a. Disturbances and eddy fluxes in Northern hemisphere flows: instability of three-dimensional January and July flows. *J. Atmos. Sci.* **40**, 836–855.

Frederiksen, J. S. 1983b. A unified three-dimensional instability theory of the onset of blocking and cyclogenesis. II: teleconnection patterns. *J. Atmos. Sci.* **39**, 969–987.

Frederiksen, J. S. 1985. The geographical locations of Southern Hemisphere storm tracks: linear theory. *J. Atmos. Sci.* **42**, 710–723.

Frederiksen, J. S. 1992. Towards a unified instability theory of large-scale atmospheric disturbances. *Trends Atmos. Sci.* **1**, 239–261.

Frederiksen, J. S. 2002. Genesis of intraseasonal oscillations and equatorial waves. *J. Atmos. Sci.* **59**, 2761–2781.

Frederiksen, J. S. and Webster, P. J. 1988. Alternative theories of atmospheric teleconnections and low-frequency fluctuations. *Rev. Geophys.* **26**, 459–494.

Frederiksen, J. S. and Bell, R. C. 1990. North Atlantic blocking during January 1979: linear theory. *Q.J.R. Meteorol. Soc.* **116**, 1289–1313.

Frederiksen, J. S. and Frederiksen, C. S. 1993a. Monsoon disturbances, intraseasonal oscillations, teleconnection patterns, blocking and storm tracks of the global atmosphere during January 1979: linear theory. *J. Atmos. Sci.* **50**, 1349–1372.

Frederiksen, J. S. and Frederiksen, C. S. 1993b. Southern Hemisphere storm tracks, blocking and low-frequency anomalies in a primitive equation model. *J. Atmos. Sci.* **50**, 3148–3163.

Frederiksen, J. S. and Frederiksen, C. S. 1997. Mechanism of the formation of intraseasonal oscillations and Australian monsoon disturbances: the roles of convection, barotropic and baroclinic instability. *Contrib. Atmos. Phys.* **70**, 39–56.

Frederiksen, J. S. and Branstator, G. 2001. Seasonal and intraseasonal variability of large-scale barotropic modes. *J. Atmos. Sci.* **58**, 50–69.

Frederiksen, J. S. and Kepert, S. M. 2006. Dynamical subgrid-scale parameterizations from direct numerical simulations. *J. Atmos. Sci.* **63**, 3006–3019.

Fyfe, J. C. 2003. Extratropical Southern Hemisphere cyclones: harbingers of climate change? *J. Climate* **16**, 2802–2805.

Fyfe, J. C., Boer, G. J. and Flato, G. M. 1999. The Arctic and Antarctic Oscillations and their projected changes under global warming. *Geophys. Res. Lett.* **26**, 1601–1604.

Hall, N. M. and Sardeshmukh, P. D. 1998. Is the time-mean Northern Hemisphere flow baroclinically unstable? *J. Atmos. Sci.* **55**, 41–56.

Hines, K. M., Bromwich, D. H. and Marshall G. J. 2000. Artificial surface pressure trends in the NCEP-NCAR reanalysis over the Southern Ocean and Antarctica. *J. Climate* **13**, 3940–3952.

IOCI 2002. *Climate variability and change in south west Western Australia*. Indian Ocean Climate Initiative Panel, Department of Environment, Water and Catchment Protection, Perth, W.A., September, 34 pp.

Kalnay, E. M., Kanamitsu, M., Kistler, R., Collins, W., Deaven, D., and co-authors 1996. The NCEP/NCAR 40-year reanalysis project. *Bull. Am. Meteorol. Soc.* **77**, 437–471.

Kållberg, P., Simmons, A., Uppala, S. and Fuentes, M. 2004. The ERA-40 Archive. ERA-40 Project Report Series No. 17, ECMWF, 18pp.

Kanamitsu, J. 1975. *On Numerical Prediction over a Global Tropical Belt*. PhD thesis, Dept of Meteor., Florida State University, Tallahassee, FL 32304, 281pp.

Kidson, J. W. 1988. Interannual variations in the Southern Hemisphere circulation. *J. Climate* **1**, 1177–1198.

Knutson, T. R. and Manabe, S. 1998. Model assessment of decadal variability and trends in the tropical Pacific Ocean. *J. Climate* **11**, 2273–2295.

Kuo, H. L. 1974. Further studies of the parameterization of the influence of cumulus convection on large scale flow. *J .Atmos. Sci.* **31**, 1232–1240.

Krishnamurti, T. N., Kanamitsu, M., Godbole, R., Chang, C. B., Carr, F., and co-authors. 1976. Study of a monsoon depression (II), Dynamical structure. *J. Meteor. Soc. Japan* **54**, 208–225.

Lee, S. 1995. Linear modes and storm tracks in a 2-level primitive equation model. *J. Atmos. Sci.* **52**, 1841–1862.

Leith, C. E. 1975. Climate response and fluctuation dissipation. *J. Atmos. Sci.* **32**, 2022–2026.

Marshall, G. J., Stott, P. A., Turner, J., Turner, W. M., King, J. C. and co-authors. 2004. Causes of exceptional atmospheric circulation changes in the Southern Hemisphere. *Geophys. Res. Lett.* **31**, L14205, doi: 10.1029/1004GL019952.

Martin, J. E. and Otkin, J. A. 2004. The rapid growth and decay of an extratropical cyclone over the central Pacific ocean. *Wea. Forecasting* **19**, 358–376.

McMurdie, L. A. and Katsaros, K. B. 1996. Satellite-derived integrated water vapour and rain intensity patterns: indicators for rapid cyclogenesis. *Wea. Forecasting* **11**, 230–245.

Meehl, G. A. and Washington, W. M. 1996. El Niño-like climate change in a model with increased atmospheric CO_2 concentration. *Nature* **382**, 56–60.

Molinari, J. 1985. A general form of Kuo's cumulus parameterization. *Mon. Wea. Rev.* **113**, 1411–1416.

Neelin, K. K., Held, I. M. and Cook, K. H. 1987. Evaporation-wind feedback and low-frequency variability in the tropical atmosphere. *J. Atmos. Sci.* **44**, 2341–2348.

Nicholls, N. 1989. Sea surface temperatures and Australian winter rainfall. *J. Climate* **2**, 965–973.

Nitta, T. and Yamada, S. 1989. Recent warming of tropical sea surface temperature and its relationship to the Northern Hemisphere circulation. *J. Meteor. Soc. Japan* **67**, 375–383.

Petty, G. W. and Miller, D. G. 1995. Satellite microwave observations of precipitation correlated with intensification rate in extratropical oceanic cyclones. *Mon. Wea. Rev.* **123**, 1904–1911.

Phillips, N. A. 1954. Energy transformations and meridional circulations associated with simple baroclinic waves in a two-level, quasi-geostrophic model. *Tellus* **6**, 273–286.

Pierrehumbert, R. T. and Swanson, K. L. 1995. Baroclinic instability. *Ann. Rev. Fluid Mech.* **27**, 419–467.

Power, S., Casey, T., Folland, C., Colman, A. and Mehta, V. 1999. Inter-decadal modulation of the impact of ENSO on Australia. *Clim. Dyn.* **15**, 319–324.

Qi, L., Leslie, L. M. and Zhao, S. X. 1999. Cut-off low pressure systems over southern Australia: climatology and case study. *Int. J. Climatol.* **19**, 1633–1649.

Roebber, P. J. 1984. Statistical analysis and updated climatology of explosive cyclones. *Mon. Wea. Rev.* **112**, 1577–1589.

Sadler, B. S., Mauger, G. W. and Stokes, R. A. 1988. The water resources implications of a drying climate in south-west Western Australia. In: *Greenhouse: Planning for Climate Change* 296–311 (ed. G.I. Pearman). Commonwealth Scientific and Industrial Research Organisation, Australia, 752 pp.

Sanders, F., and Gyakum, J. R. 1980. Synoptic-dynamic climatology of the "bomb". *Mon. Wea. Rev.* **108**, 1589–1606.

Simmonds, I. and Keay, K. 2000a. Variability of Southern Hemisphere extratropical cyclone behavior, 1958–97. *J. Climate* **13**, 550–561.

Simmonds, I. and Keay, K. 2000b. Mean Southern Hemisphere extratropical cyclone behavior in the 40-year NCEP-NCAR reanalysis. *J. Climate* **13**, 873–885.

Simmons, A. J., Wallace, J. M. and Branstator, G. W. 1983. Barotropic wave propagation and instability, and atmospheric teleconnection patterns. *J. Atmos. Sci.* **40**, 1363–1392.

Simmons, A. J., da Costa Bechtold, V., Beljaars, A. C. M., Kållberg, P. W. and co-authors 2004. Comparison of trends and low-frequency variability in CRU, ERA-40, and NCEP/NCAR analysis of surface air temperature. *J. Geophys. Res.* **109**, D24115, doi:1029/2004JD005306.

Smith, I. N. 1994. Indian Ocean sea-surface temperature patterns and Australian winter rainfall. *Int. J. Climatol.* **14**, 287–305.

Smith, I. N. 2004. Trends in Australian rainfall – are they unusual? *Aust. Met. Mag.* **53**, 163–173.

Smith, I. N., McIntosh, P., Ansell, T. J., Reason, C. J. C. and McInnes, K. 2000. South-west Western Australian winter rainfall and its association with Indian Ocean climate variability. *Int. J. Climatol.* **20**, 1913–1930.

Trenberth, K. E. 1981. Observed Southern hemisphere eddy statistics at 500 mb: frequency and spatial dependence. *J. Atmos. Sci.* **38**, 2585–2605.

Trenberth, K. E. 1990. Recent observed interdecadal climate changes in the Northern Hemisphere. *Bull. Amer. Meteor. Soc.* **71**, 988–993.

Trenberth, K. E. 1991. Storm tracks in the Southern Hemisphere. *J. Atmos. Sci.* **48**, 2159–2178.

Whitaker, J. S. and Barcilon, A. 1992. Type B cyclogenesis in a zonally varying flow. *J. Atmos. Sci.* **49**, 1877–1862.

Whitaker, J. S. and Dole, R. M. 1995. Organization of storm tracks in a zonally varying flow. *J. Atmos. Sci.* **52**, 1178–1191.

Zhang, Y., Wallace, J. M. and Battisti, D. S. 1997. ENSO-like variability: 1900–93. *J. Climate* **10**, 1004–1020.